The final publication is available at

https://doi.org/10.1016/j.clay.2019.105352

A comparative photocatalytic study of TiO$_2$ loaded on three natural clays with different morphologies

Aichun Wu[1], Duoxiao Wang[1], Chao Wei[1], Xudong Zhang[2], Zhangsheng Liu[1], Peizhong Feng[1], Xuemei Ou[1], Yinghuai Qiang[1], Hermenegildo Garcia[3], Jinan Niu[1*]

[1]School of Materials Science and Engineering, China University of Mining and Technology, Xuzhou 221116, P. R. China

[2] Earth Moving Machinery Business Unit, Xuzhou Construction Machinery Group Co., Ltd. Xuzhou 221000, P. R. China

[3]Instituto de Tecnologia Quimica CSIC-UPV, Universitat Politecnica de Valencia, Valencia 46022, Spain

Corresponding author: Jinan Niu

School of Materials Science and Engineering, China University of Mining and Technology, Xuzhou 221116, P. R. China

Email: jinan.niu@cumt.edu.cn (J. Niu)

Abstract

In this work, a sol-gel method was used to load TiO_2 nanoparticles on three clays (kaolinite, halloysite and palygorskite) with different morphologies (plates, tubes, and rods with micro tunnels), and then the photocatalytic performance of obtained clay-TiO_2 composites for degradation of methyl orange was comparatively investigated. The results surprisingly show that the trend of photocatalytic performance of composites is opposite to that of special surface area of corresponding clays. By concentrated analysis of the loading status of TiO_2, the lowest photocatalytic efficiency of palygorskite-TiO_2 composite is mainly ascribed to the aggregation of TiO_2 nanoparticles on Pal surface, not the amount of TiO_2. The more disperse distributions of TiO_2 on two kaolinite (001) surfaces and halloysite outer surface results in the better photocatalytic performance of kaolinite-TiO_2 and halloysite-TiO_2 composites than that of palygorskite-TiO_2 composite. The strong adsorption of sulfonate group of methyl orange on kaolinite hydroxyl surface leads to the better photocatalytic performance of kaolinite-TiO_2 composite than halloysite-TiO_2 composite. This study can provide a direct guidance to select appropriate clay-photocatalyst composites for different practical applications.

Keywords: kaolinite, halloysite, palygorskite, surface structure, loadability, photocatalysis.

1. Introduction

Due to multiple advantages e.g. high chemical stability, large specific surface area and abundant active sites, nano TiO_2 is widely used in photocatalytic degradation of organic pollutant (Murgolo et al., 2015), purification of exhaust gas (Akhter et al., 2015), reduction of heavy metal ions (Wang et al., 2017), water splitting (Singh and Dutta, 2018), antibacterial (Fagan et al., 2016), solar cells (Wang et al., 2014) and gas sensors (Zhang et al., 2010). However, two urgent problems exist during sewage treatment. One is the aggregation of TiO_2 nanoparticles with high Gibbs free energy resulting in decrease of the number of active sites; the other is the trouble to separate and recover nano TiO_2 in water. TiO_2 nanoparticles can be loaded on some supports to improve their dispersion and recovery, such as glass fabric (Palau et al., 2012), molecular sieves (Hsien et al., 2001; Mahalakshmi et al., 2009), activated carbon (Zhang et al., 2005), graphene/carbon composite (Kim et al., 2012), carbon fiber (Meng et al., 2014) and FTO conductive glass (Oliveira et al., 2010) etc.. However, these supports are generally artificial and high-cost, limiting the practical applications of such composite photocatalysts.

Natural clays have been widely used in supporting nano TiO_2 for photodegradation of organic pollutants in water due to their large reserves, wide distribution and low cost. For instance, kaolinite loading TiO_2 has been applied to degrade Congo red (Chong et al., 2009), red G and 4-nitrophenol (Zhang et al., 2011a), acid orange 7 (Mamulová Kutláková et al., 2011); rectorite has been adopted to support TiO_2 for removal of acid red G and 4-nitrophenol (Zhang et al., 2011b); palygorskite loading TiO_2 has been used to degrade methylene blue (Zhao et al., 2006). The more examples have been outlined in a recently comprehensive review with respect to clays loading TiO_2 towards photocatalysis (Szczepanik, 2017). Different clays possess diverse surface structures and properties which may produce different loadability of photocatalysts, and also, different clay minerals have different reserves and accessibilities which are directly related to the cost of clays and can

determine the scope of specific applications of clay-photocatalyst composites. Therefore, it is necessary to carry out comparative experiments regarding various clays loading photocatalysts, with a view to providing direct guidance for the practical applications of clay-photocatalyst composites. This is particularly important for large-scale environmental restoration using photocatalytic technology, in which the balance between photocatalytic performance and cost of catalysts is often carefully considered. However, no comparative researches about different clays loading TiO_2 nanoparticles by means of the same method towards photocatalytic degradation of organic pollutants in water have been found until now. Different research groups often use different load methods and evaluation criteria, so that it is difficult to directly compare these results. An additional benefit to perform such comparative researches is to provide some basic information about surface structure of clays which can be directly reflected in loading behavior of catalysts and finally photocatalytic performance of composites.

In this work, the loading of nano TiO_2 was carried out on three clays: kaolinite (Kaol), halloysite (Hal) and palygorskite (Pal). These three clays have typical plate, tube and rod morphologies with different specific surface area, respectively. The surface structures of clays can lead to distinct adsorption and supporting capabilities which thus are conducive to mutual comparison between clays. Generally, Pal and Hal have larger specific surface area due to their abundant pore structure, so they should support more TiO_2 nanoparticles and adsorb more pollutant molecules, which would bring on better photocatalytic performance. Surprisingly, the results here show that kaolinite-TiO_2 composite has the best photocatalytic activity for degradation of methyl orange (MO) dye, while kaolinite has the smallest SSA in three clays. Through comparative analysis of structures, morphologies and loadabilities of clays, the causes of difference in photocatalytic performance of clay-TiO_2 (CT) composites was explained in detail.

2. Experimental

2.1 Materials

Raw Kaol, Hal and Pal are from Maoming in Guangdong province, Lingshou in Hebei province, and Xuyi in Jiangsu province, separately. Their major composition (wt % in oxides) were determined by X-ray fluorescence spectroscopy (XRF), as shown in Table S1. Nitric acid, isopropanol and tetrabutyl titanate are of analytical grade, purchased from Sinopharm Chemical Reagent Co., Ltd (Shanghai).

2.2 Preparation

Sol-gel method was used to load nano TiO_2 on clay surface (Li et al., 2015; Niu et al., 2018). Briefly, 15 ml isopropanol, 5 ml nitric acid (2 mol/L) and 1ml tetrabutyl titanate were first mixed and stirred at room temperature for 1 h to transparent; next, deionized water was added to the solution to a total volume of 250 ml; then, 1 g clay was added into the solution, followed by magnetic stirring at 65 °C for 24 hours. After reaction, the white precipitate was separated by centrifugation at 5000 rpm for 5 min and then dried at 80 °C overnight. The obtained clay-TiO_2 (CT) composites are denoted as KT (kaolinite-TiO_2), HT (halloysite-TiO_2) and PT (polykorskite-TiO_2), respectively.

2.3. Characterization

The phases of the obtained samples were characterized by X-ray Diffraction (XRD, D8 Advance, Bruker) with Cu Kα radiation at 40 kV and 30 mA. The morphology was examined by field emission scanning electron microscope (SEM, UHR SU8220, Hitachi) and transmission electron microscope (TEM, Tecnai G2 F20, FEI). The content of TiO_2 in CTs was analyzed by X-ray fluorescence spectrometer (XRF, S8 TIGER, Bruker). The specific surface area (SSA) and pore size distribution (PSD) of samples was measured by an accelerated surface area and porosimetry system (ASAP 2020 plus HD88, Micromeritics) under liquid nitrogen temperature (77.3 K).

2.4 Photocatalytic measurement

The photocatalytic activity of CTs was evaluated in degradation of MO dye under simulated sunlight irradiation at 25 °C. 20 mg of samples were suspended in 20

ml of 10 mg/L MO aqueous solution. Before photodegradation tests under water-cooled xenon lamp irradiation with 500 W power, the suspension was stirred in the dark for 1 h. Then, 2 ml of suspension was taken out at 30 minute intervals, and the solid was separated from the solution by centrifugation (10000 rpm, 5 min). The remaining clear liquid was used for absorbance measurements at a wavelength of 464 nm on a UV–visible spectrophotometer (T6-1650F, Beijing Persee).

3. Results and discussion

3.1 XRD analysis

The XRD patterns of three clays before and after loading TiO_2 are shown in Fig.1. In order to facilitate mutual comparison for different samples, the background of all curves has been subtracted. Kaol shows high crystallinity with the Hinckley index of 0.81 (Hinckley, 1962). Hal exhibits the typical pattern of dehydrated halloysite with (001) basal reflection at 12.1 ° (0.73 nm), which is further confirmed by (100) and (002) reflections at 19.9 and 24.7 ° (Wang et al., 2013). Both of Kaol and Hal show relatively high purity and no obvious impurity can be detected. For Pal sample, the strongest reflection at 8.39 ° corresponds to (110) plane with 1.05 nm spacing, while the reflections at 16.4, 19.8, 20.8, 21.5, 24.1 and 26.6 ° agree with (130), (040), (121), (310), (221) and (231) planes of palygorskite (PDF No. 31-0783). After loading TiO_2, the XRD pattern shape and the reflection positions of clays do not change obviously. For further comparison, the patterns of all samples were normalized and overlapped (inset of Fig.1). Through local enlargement in 23-28 ° range, a new reflection at 25.28 ° are found for all CT composites, which is consistent with (101) plane of anatase TiO_2, according to the previous experimental results (Li et al., 2013; Niu et al., 2018). This result clearly reveals the successful formation of CT composites by means of sol-gel method. Furthermore, it can be seen from Fig.1 that the increase of reflection at 25.28 ° caused by the TiO_2 formation on Hal and Pal is more obvious than on Kal, suggesting more anatase TiO_2 generated on Hal and Pal surfaces.
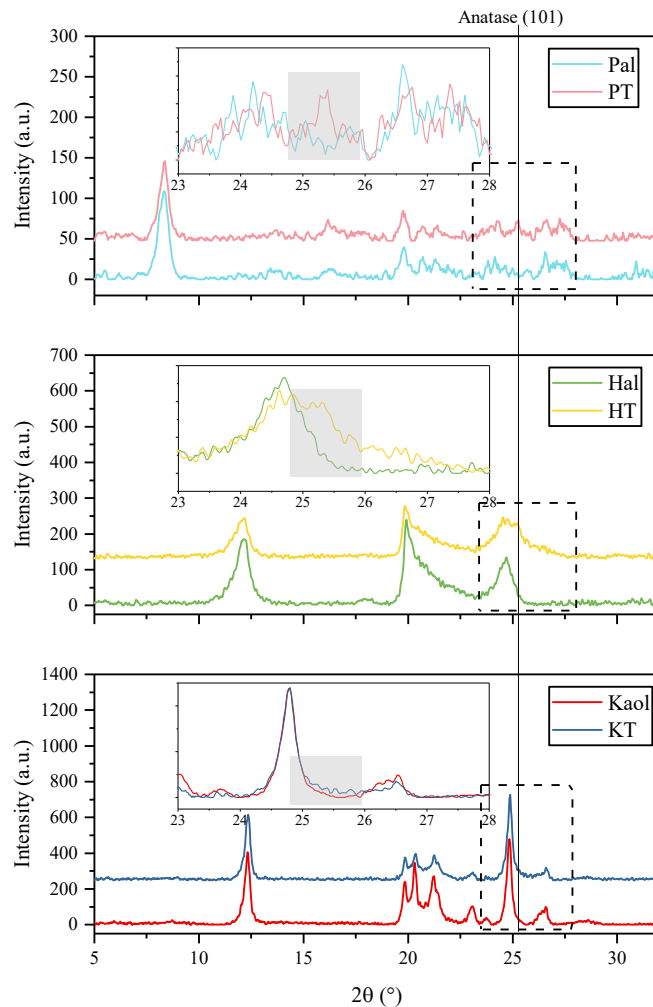
Fig.1. XRD patterns of Kaol, KT, Hal, HT, Pal and PT.

3.2 SEM analysis

The SEM comparasion of three clays before and after loading TiO_2 are given in Fig.2. Before loading, Kaol shows well-shaped pseudo-hexagonal plates with the width range of 0.2-3 μm (Fig.2a1). Hal shows typical tubular structure with the length range of 500-1000 nm and the diameter range of 80-200 nm (Fig.2b1). In some Hal tubes, hollow structure can be obviously seen at the end (as marked by red dotted circle). Pal shows nano rods with the length range of 200-1500 nm and the diameter range of 15-40 nm (Fig.2c1). The surface of each kind of clay particles is rather smooth and no obvious small particles can be found. After loading TiO_2, the characteristic shape of clay particles did not change significantly, indicating that the loading process does not damage clay structures, corresponding to the XRD results.

7

Nano particles occuring on clay surfaces indicate that the sol-gel method can be adopted to well load TiO_2 on clay surfaces (Fig.a2-c2). Relatively speaking, the load of nano TiO_2 on Kaol and Hal surfaces is more uniform only with occasionally large particles, while TiO_2 on Pal surface shows more aggregates with the size range of 30-200 nm (Fig.c2). The different forms of TiO_2 existence on clays can be attributed to the distinct surface properties of each clay, which will be discussed further later.
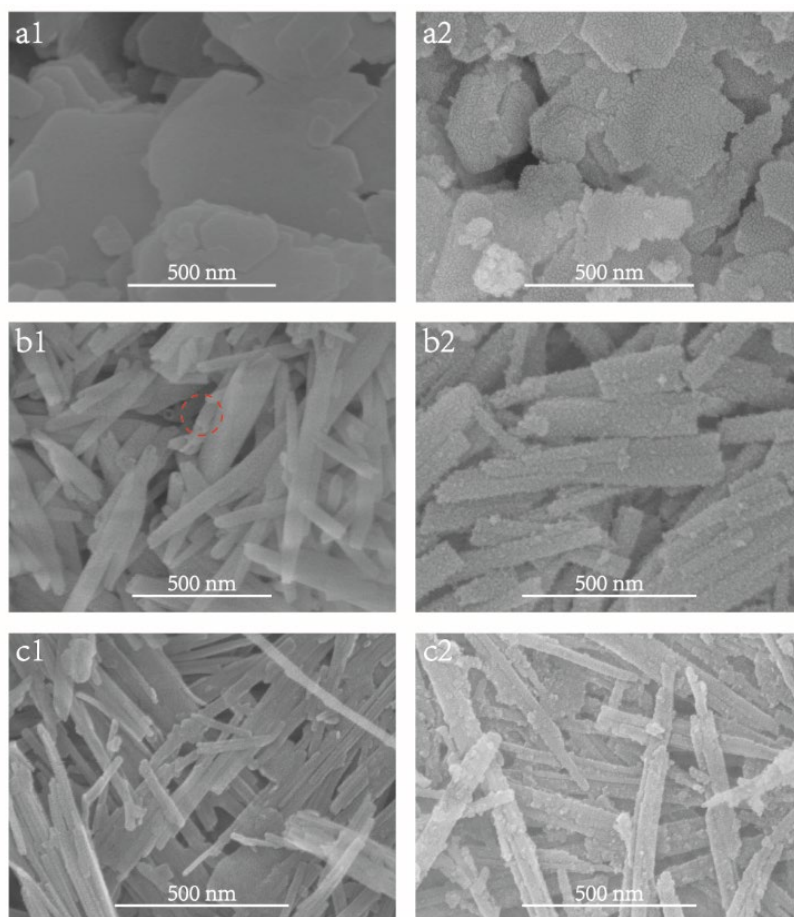
Fig.2. SEM images of (a1) Kaol, (a2) KT, (b1) Hal, (b2) HT, (c1) Pal and (c2) PT.

3.3 TEM analysis

TEM measurements were performed to further investigate the distribution of TiO_2 on clay surface (Fig.3). The images in Fig.3a1-c1 confirm the characteristic morphologies of pseudo-hexagonal plate, tube and rod for Kaol, Hal and Pal, respectively. The inner diameter range of Hal is 12-30 nm. Pal consists of some approximately parallel strips, which can be clearly seen from the local enlargement (Fig.S1). For CT composites, more uniform distribution of TiO_2 on Kaol and Hal

surfaces than that on Pal can be seen (Fig.3a2-c2), agreeing with the SEM results. Moreover, the inner surface of Hal nanotubes still remains smooth in contrast to the rough outer surface, suggesting that TiO_2 nanoparticles are mainly formed on the out surface of Hal nanotubes (Fig.3d). High resolution TEM (HRTEM) results show that the size of TiO_2 on Kaol surface is about 5 nm (Fig.3e), similar to those on other two clays (Fig.S2 and S3). The lattice diffraction fringe of 0.35 nm corresponds to (101) spacing of anatase TiO_2, in accordance with the XRD results, which further confirm the successful load of TiO_2 on clay surfaces by a facile sol-gel method.
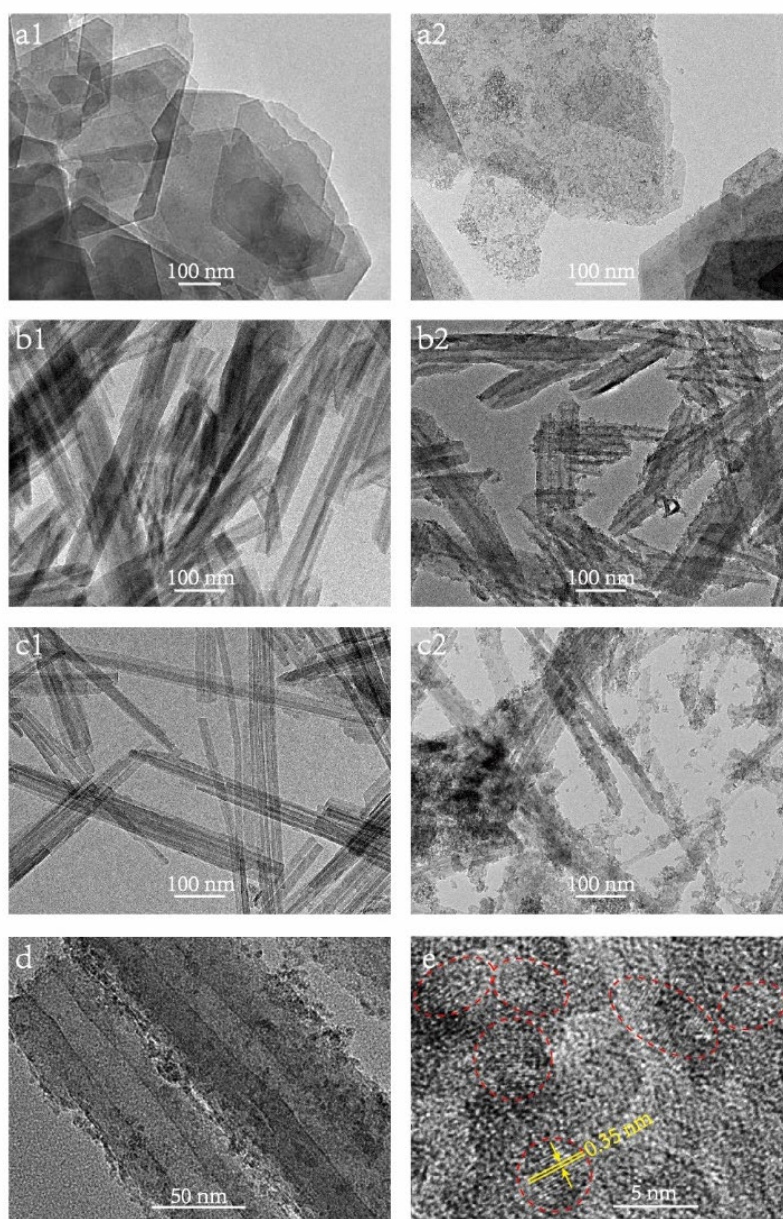
Fig.3. TEM images of (a1) Kaol, (a2) KT, (b1) Hal, (b2) HT, (c1)Pal, (c2) PT and (d) HRTEM image of a local in KT.

3.4 Specific surface area and pore size distribution

The SSA and PSD of samples was obtained by measuring nitrogen absorption-desorption isotherms under low temperature (77 K) (Fig.4). The adsorption isotherm of Kaol shows typical Type II characteristic according to the IUPAC classification, and the hysteresis loop of desorption isotherm is minor, agreeing with the previous report (Yuan et al., 2013) (Fig.4a1). For Hal and Pal, their adsorption isotherms belong to Type IV, and the descending part of their hysteresis loops is near parallel to adsorption isotherms, revealing existence of slender tunnels with open ends, corresponding to the structural features of these two clays (Brigatti et al., 2013) (Fig.4b1 and c1). After loading TiO_2, the quantity of N_2 adsorbed on samples increases accompanied with upward movement of the isotherms and slight increment of hysteresis. The PSD curves of samples calculated by the Barrett-Joyner-Halenda (BJH) method (Fig.4a2-c2) show a main peak centered at 4 nm for Kaol which may be caused by tensile strength effect (TSE) (Groen et al., 2003). For Hal, a new peak at about 18 nm also occurs besides 4 nm peak, corresponding to Hal hollow nanotubes in agreement with the TEM results. For Pal, the TSE peak at about 4 nm is main as well. However, the intensity of PSD curve below 10 nm is obviously stronger than that for Kaol, the reason is that the actual PSD in Pal is just in this range and thus overlaps with original TSE peak. After loading TiO_2, all PSDs in the range below 20 nm increase, possibly led by the interspace among TiO_2 nanoparticles on clays. Among three raw clays, Pal has the largest SSA, reaching 129.70 m^2/g which can be attributed to abundant micropores in Pal; Hal has much larger SSA (60.27 m^2/g) than Kaol (18.03m^2/g), because the walls of Hal tubes are usually thinner than Kaol plates resulting more interlayer surface exposed (Joussein et al., 2005). Through loading TiO_2, the SSA of all three clays significantly increases, reaching 193.86, 124.33 and 63.19 m^2/g for PT, HT and KT, respectively, mainly due to the newly formed surface of TiO_2 nanoparticles.
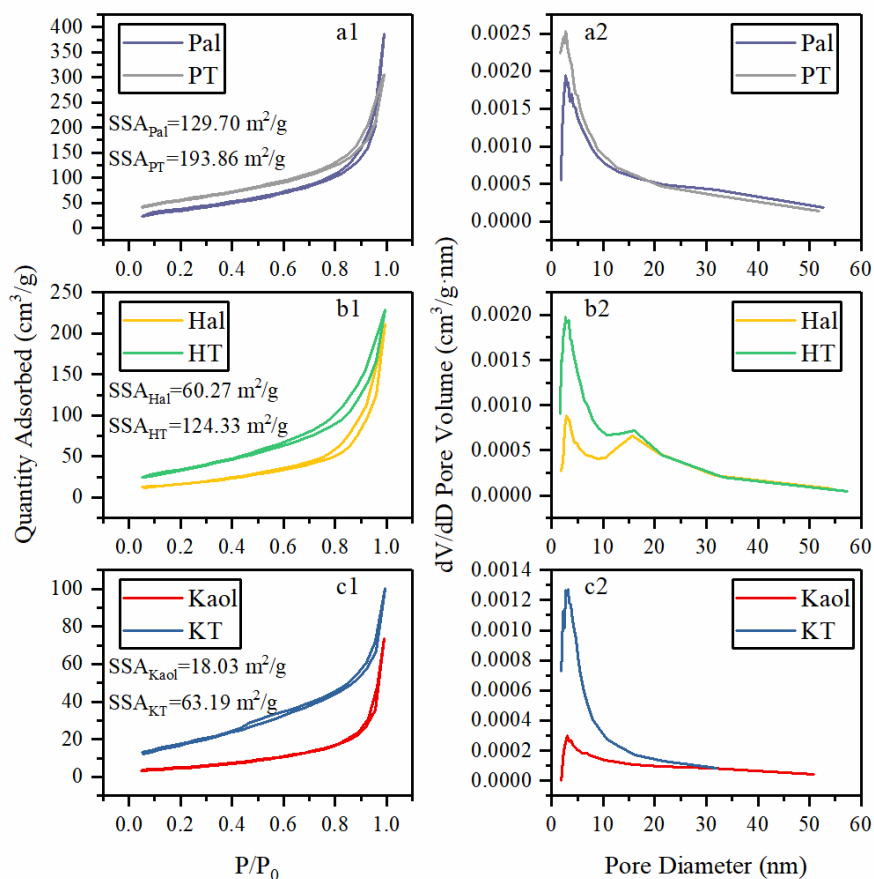
Fig.4. Nitrogen absorption-desorption isotherms (a1-c1), and pore size distribution (a2-c2) for Kaol, KT, Hal, HT, Pal and PT.

3.5 Photocatalytic activity

The photocatalytic activity of clays before and after loading TiO_2 was investigated by decolorization of MO under simulated sunlight irradiation. Three groups of independent photocatalytic experiments were performed to check the reliability of photocatalytic results (Fig.S4), in which samples from each group were re-prepared and all samples from a group were measured under the same irradiation with the multi-station reactor. Three sets of results show the similar trend and their average is shown in Fig.5a. When without samples as catalysts, the concentration of MO decreases slightly in the whole reaction period. However, the concentration of MO decreases significantly when using CT composites, indicating good photocatalytic activity induced by TiO_2 nanoparticles. In all three CT composites, KT exhibits excellent photodegradability towards MO, even better than HT and PT with

11

240 larger SSA. In order to compare the photocatalytic performance of samples more

241 clearly, the histogram of primary reaction rate constants is shown in Fig.5b. It can be

242 easily seen that raw clays have similar and weak photocatalytic performance with

243 comparable degradation ratios with blank solution, while KT, HT and PT have the

244 obviously increased performance, in which KT has the highest rate constant (0.01207

245 min^{-1}) that is 1.7 and 3.0 times the rate constants of HT (0.00704 min^{-1}) and PT

246 (0.00406 min^{-1}), respectively. This result leads to a perplexing question: Kaol, Hal and

247 Pal are all phyllosilicate and should have loadabilities for TiO_2 in keeping with their

248 SSA values and then give a photocatalytic trend of KT<HT<PT, but the actual result

249 is just the opposite. Why is this so?
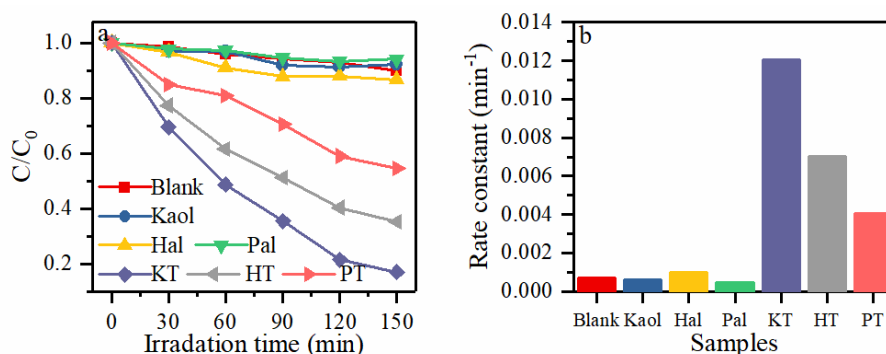
250

251 Fig.5. Photocatalytic activity of Kaol, KT, Hal, HT, Pal, PT and blank reference. (a) Degradation

252 kinetic curve; (b) Rate constant.

253 4 Discussion

254 To explain the inconsistency of the trend of photocatalytic performance of CTs

255 with the trend of SSA of corresponding clays, here the load status of TiO_2 on clays is

256 focused on and discussed in detail, which has been proved to play an important role

257 on photocatalytic performance (Egerton and Tooley, 2004). The difference in surface

258 structure details of clays can result in the distribution difference of TiO_2 on clays and

259 then the divergence of photocatalytic performance of CTs.

260 Firstly, the contents of TiO_2 in CTs (ω_T) are compared, as given in Table 1. It can

261 be seen that three clays have distinct loads of TiO_2 with the order of Pal>Hal>Kaol, in

262 agreement with the SSA order of clays. This result should be attributed to the number

263 of surface active sites of clays for nucleation of TiO_2. However, it exacerbates the

264   conflict between the trends of SSA and photocatalytic performance. PT has the most

265   TiO$_2$ but the worst photocatalytic performance; while KT has the least TiO$_2$ and the

266   best photocatalytic performance. This result suggests that the difference among

267   photocatalytic performance of three CTs is not simply determined by the amount of

268   TiO$_2$ loaded on clays.

269   Table 1: the loading state of TiO$_2$ on KT, HT and PT

Samples	KT	HT	PT
Loading content of TiO$_2$ in CT composites, ω_T（wt.%）	11.11	14.57	20.04
Loading efficiency of clays for TiO$_2$, η_{load} (mg/m^2)	6.9	2.8	1.9
Aggregation degree of TiO$_2$ loaded on clays, α (mg/m^2)	2.8	2.7	3.9

270

271   Next, the amount of TiO$_2$ loaded on per unit area of clays are calculated to

272   evaluate the loading efficiency of clays for TiO$_2$ (η_{load}). Suppose TiO$_2$ nanoparticles

273   uniformly cover clay surface, the η_{load} can be denoted as Equation 1:

274    $$\eta_{load} = \frac{W_T}{S_C} = \frac{\omega_T}{S_C(1-\omega_T)} \quad (1)$$

275   in which, S_C is the surface area of per gram of clay (i.e. SSA), W_T is the TiO$_2$ mass

276   loaded on per gram of clay, calculated by the content of TiO$_2$ in CT composite,

277   equaling $\omega_T/(1-\omega_T)$. The η_{load} reflects the nucleation and attachment ability of TiO$_2$ on

278   clay surface in the sol-gel process. The results in Table 1 indicate that Kaol surface

279   has the highest loading efficiency of TiO$_2$, reaching 6.9 mg/m^2, compared to Hal's 2.8

280   mg/m^2 and Pal's 1.9 mg/m^2. Hal and Pal with larger SSAs have lower load efficiency

281   of TiO$_2$, due to that a large part of SSAs of Hal and Pal come from the contribution of

282   inner surface for which it is not easy to load TiO$_2$ nanoparticles because the precursor

283   species of TiO$_2$ in the sol-gel reaction are difficult to enter the holes in clays owing to

284   space constraints. The smooth inner surface of Hal tubes in HT further confirms this

285   point (Fig.3d). Note that although Kaol has the relatively high η_{load}, the absolute

286   amount of TiO$_2$ on Kaol is still lower than that on Hal and Pal, because less particles

287   are included in unit mass of clay due to their larger size than Hal and Pal's (Fig.2 and

288   Fig.3), resulting in less practical surface for loading TiO_2 in Kaol. Similarly, the

289   particle size of Pal is also smaller than Hal, leading to the more TiO_2 on Pal.

290   For Kaol, the loading efficiency of its two different basal surfaces can be

291   discussed as well. When ignoring the adsorption effect of lateral surface, the total

292   loading efficiency of Kaol (η_K) can be represented through dividing the total amount

293   of TiO_2 on basal surfaces by the area sum of basal surfaces (Equation 2):

294    $$\eta_K = \frac{W_{T-K}}{S_K} \approx \frac{W_{T-OH}+W_{T-SiO}}{S_{OH}+S_{SiO}} = \frac{W_{T-OH}+W_{T-SiO}}{2S_{001}} = \frac{1}{2}\left(\frac{W_{T-OH}}{S_{001}} + \frac{W_{T-SiO}}{S_{001}}\right) = \frac{1}{2}\left(\eta_{OH} + \eta_{SiO}\right)$$

295   (2)

296   where W_{T-K} is the total mass of TiO_2 on per gram of Kaol, S_K is the total SSA value of

297   Kaol, W_{T-OH} is the mass of TiO_2 on hydroxyl surface and W_{T-SiO} is the mass of TiO_2 on

298   silicon-oxygen surface of per gram of Kaol,， approximately, $W_{T-K}=W_{T-OH}+W_{T-SiO}$; S_{OH}

299   is the SSA of hydroxyl surface, S_{SiO} is the SSA of silicon-oxygen surface, obviously,

300    $S_{OH}=S_{SiO}= S_{001}$ (S_{001} is the SSA of single (001) surface), then $S_K \approx S_{OH}+S_{SiO}=2S_{001}$. The

301   η_{OH} and η_{SiO} are the loading efficiency of hydroxyl surface and silicon-oxygen surface,

302   respectively. From the Equation 2, it can be clearly seen that the total loading

303   efficiency of Kaol is approximated as the geometric mean of loading efficiency of

304   hydroxyl surface and silicon-oxygen surface.

305   Due to the same structure of clay layer, the silicon-oxygen surface of Kaol

306   should have the equivalent loading state of TiO_2 to the outer surface of Hal tubes.

307   Consequently, the η_{SiO} of Kaol can be deduced according to the loading efficiency of

308   outer surface of Hal. Because the inner surface of Hal tubes does not load TiO_2

309   (Fig.3d), the η_{load} of Hal in Table 1 can be recalculated to 5.6 mg/m^2 according to half

310   of the measured SSA, actually reflecting the loading efficiency of outer surface of Hal

311   as well as that of silicon-oxygen surface of Kaol. Then the η_{OH} of Kaol obtained

312   through Equation 2 is 8.2 mg/m^2. The definite η_{load} values for both basal surfaces of

313   Kaol confirm the loading of TiO_2 on the silicon-oxygen surface and the hydroxyl

314   surface, and the η_{load} of hydroxyl surface may be slightly higher than that of

315   silicon-oxygen surface, as the hydroxyls are easier to condensate with hydrolyzed

316 products of Ti salt, e.g. $Ti(OH)_x$ to form a strong bond (Chen et al., 2003).

317 Then, the agglomeration degree (α) of TiO_2 loaded on clay surface is evaluated.

318 The greater the agglomeration degree, the less the proportion of outer TiO_2 actually

319 undergoing photocatalytic reaction and the lower the final photocatalytic efficiency.

320 Suppose the increase of SSA of CT is only contributed by TiO_2, then α can be

321 calculated by Equation 3:

322 $$\alpha = \frac{W_T}{S_T} = \frac{\omega_T}{S_{CT} - S_C(1 - \omega_T)} \quad (3)$$

323 where S_T is the newly formed SSA due to TiO_2, S_{CT} is the SSA of CT composites. α

324 represents the agglomeration of TiO_2 on per unit area of clay, mainly reflecting its

325 own property and therefore having an obvious reference meaning. The results in Table

326 1 show that the α of TiO_2 on Kaol and Hal are very similar (2.8 and 2.7 mg/m^2,

327 separately), both of which are significantly lower than that of TiO_2 on Pal (3.9 mg/m^2).

328 This phenomenon is consistent with the results of SEM and TEM (Fig.2 and 3). It

329 may be for this reason that the effective surface active sites of TiO_2 are reduced, so

330 that the PT composite exhibits lower photocatalytic activity when with the higher

331 TiO_2 content.

332 The high α of TiO_2 on PT is mainly contributed to special gully structure of Pal

333 surface. Unlike the relatively dense and uniform atom arrangement in Kaol and Hal

334 surfaces, Pal surface is made up of 2:1 clay layer strips and gaps, constructing many

335 steps (Fig.6). When nucleation occurs at these steps through the hydrolysis of Ti salt,

336 not only the hydroxyl groups on the side of the step can be utilized for

337 polycondensation, but also the bottom can be touched, facilitating the preferential

338 nucleation. This case is very similar to the spiral dislocation nucleation during

339 material solidification (Bauser and Strunk, 1981). Such concentrated nucleation at the

340 steps will form the aggregation of TiO_2. Kaol or Hal does not have this type of

341 nucleation sites, so the nucleation on their surfaces is more uniform.
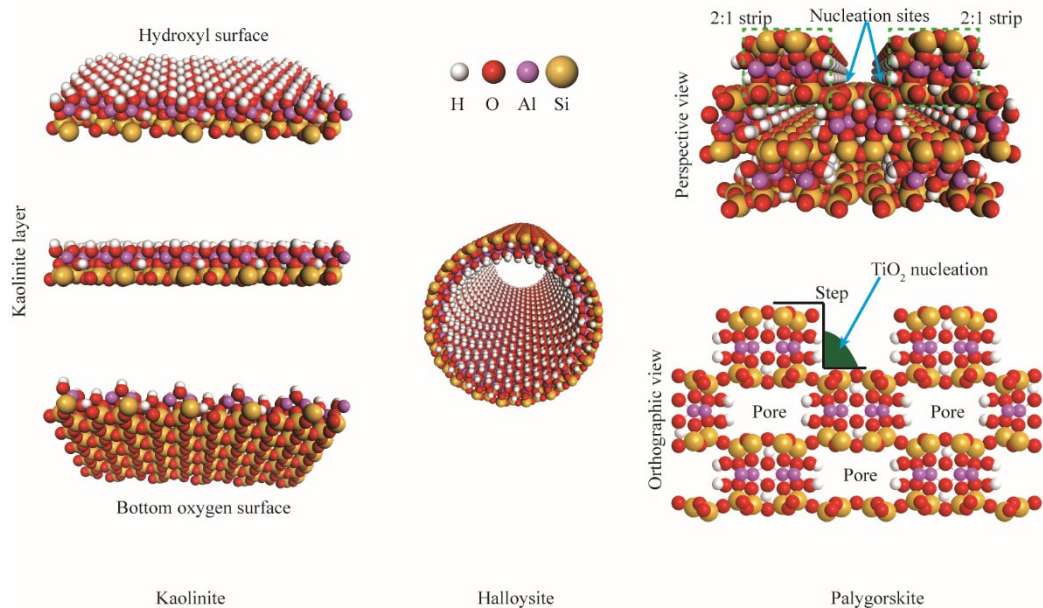
Fig.6 Comparison between surface structures of kaolinite, halloysite and palygorskite.
The nucleation sites of TiO_2 are also marked for palygorskite.

Finally, the difference between photocatalytic performance of KT and HT is discussed. The α values of TiO_2 in KT and HT are similar. However, the actual amount of TiO_2 in HT is more than that in KT, so it is difficult to explain why KT has the better photocatalytic performance than HT, only based on the perspective of TiO_2 agglomeration. It is noted that the sulfonate group in MO molecule is negatively charged (Fig. 7), and the hydrogen in hydroxyl surface is electropositive which can adsorb the sulfonate group through Coulomb force or hydrogen bonding. After loading TiO_2 on hydroxyl surface of Kaol, these uncovered hydroxyl will adsorb the sulfonate, facilitating the photocatalytic degradation of MO dye around TiO_2. Consequently, the photocatalytic efficiency of KT composite is greatly improved. For Hal, TiO_2 nanoparticles are mainly loaded on silicon-oxygen surface, the bottom oxygen in which is electronegative and thus does not have such adsorption to the sulfonate, resulting in the lower photocatalytic degradation of MO.
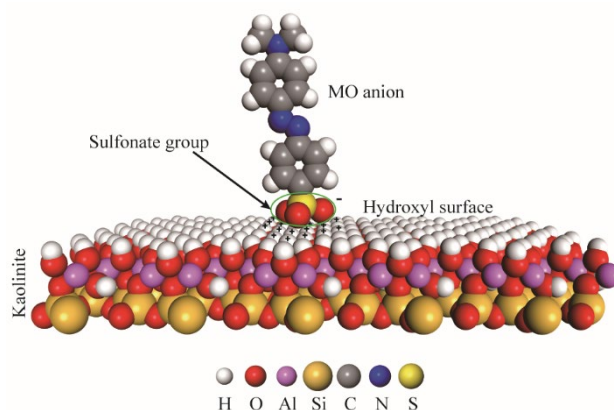
Fig.7 Schematic diagram of adsorption of MO on hydroxyl surface of kaolinite

5 Conclusion

In this work, TiO_2 nanoparticles were loaded on three clays (kaolinite, halloysite and palygorskite) with distinct micro morphologies (plates, tubes, and rods with micro tunnels) by means of the sol-gel method, and the photocatalytic performance for degradation of MO dye was comparatively investigated for obtained CT composites. The results are as follows:

(1) the photocatalytic performance of composites shows a different trend from special surface area of corresponding clays.

(2) the amount of TiO_2 loaded on clay surfaces shows a trend of Kaol<Hal<Pal, which is consistent with that of the SSA of clays with respect to the accessible active sites for TiO_2 nucleation.

(3) the loading efficiency of clay surfaces gives a trend of Kaol>Hal>Pal, attributing to no load in the Hal tubes and in the Pal tunnels leading to reduced available surface for loading TiO_2.

(4) the order of the aggregation degree of TiO_2 on clay surfaces is Kaol≈Hal>Pal. The reason can be that the gully structure of Pal surface causes aggregated nucleation at the steps, compared to the relatively uniform atom arrangement in Kaol and Hal surfaces.

(5) the hydroxyl surface of Kaol can adsorb the sulfonate group of MO anion, facilitating photocatalytic reaction between MO and nearby TiO_2 on (001) hydroxyl surface.

17

Overall, the aggregation of TiO_2 on Pal surface, the no-load of TiO_2 in Hal tubes and the adsorption of MO on hydroxyl surface of Kaol attribute to the inconsistency of the trend of photocatalytic performance with that of SSA of clays, focally from the perspective of load status of TiO_2.

Acknowledgement

References

Akhter, P., Hussain, M., Saracco, G., Russo, N., 2015. Novel nanostructured-TiO_2 materials for the photocatalytic reduction of CO_2 greenhouse gas to hydrocarbons and syngas. Fuel 149, 55–65. https://doi.org/10.1016/j.fuel.2014.09.079

Bauser, E., Strunk, H., 1981. Analysis of dislocations creating monomolecular growth steps. J. Cryst. Growth 51, 362–366. https://doi.org/10.1016/0022-0248(81)90321-3

Brigatti, M.F., Galán, E., Theng, B.K.G., 2013. Structure and Mineralogy of Clay Minerals, in: Developments in Clay Science. pp. 21–81. https://doi.org/10.1016/B978-0-08-098258-8.00002-X

Chen, Y.-F., Lee, C.-Y., Yeng, M.-Y., Chiu, H.-T., 2003. The effect of calcination temperature on the crystallinity of TiO_2 nanopowders. J. Cryst. Growth 247, 363–370. https://doi.org/10.1016/S0022-0248(02)01938-3

Chong, M.N., Vimonses, V., Lei, S., Jin, B., Chow, C., Saint, C., 2009. Synthesis and characterisation of novel titania impregnated kaolinite nano-photocatalyst. Microporous Mesoporous Mater. 117, 233–242. https://doi.org/10.1016/j.micromeso.2008.06.039

Egerton, T.A., Tooley, I.R., 2004. Effect of changes in TiO_2 dispersion on its

410   measured photocatalytic activity. J. Phys. Chem. B 108, 5066–5072.

411   https://doi.org/10.1021/jp0378992

412 Fagan, R., McCormack, D.E., Dionysiou, D.D., Pillai, S.C., 2016. A review of solar

413   and visible light active TiO_2 photocatalysis for treating bacteria, cyanotoxins and

414   contaminants of emerging concern. Mater. Sci. Semicond. Process. 42, 2–14.

415   https://doi.org/10.1016/j.mssp.2015.07.052

416 Groen, J.C., Peffer, L.A.A., Pérez-Ramírez, J., 2003. Pore size determination in

417   modified micro- and mesoporous materials. Pitfalls and limitations in gas

418   adsorption data analysis. Microporous Mesoporous Mater. 60, 1–17.

419   https://doi.org/10.1016/S1387-1811(03)00339-1

420 Hinckley, D.N., 1962. Variability in "crystallinity" values among the kaolin deposits

421   of the coastal plain of georgia and south carolina. Clays Clay Miner. 11, 229–235.

422   https://doi.org/10.1346/CCMN.1962.0110122

423 Hsien, Y.-H., Chang, C.-F., Chen, Y.-H., Cheng, S., 2001. Photodegradation of

424   aromatic pollutants in water over TiO_2 supported on molecular sieves. Appl.

425   Catal. B Environ. 31, 241–249. https://doi.org/10.1016/S0926-3373(00)00283-6

426 Joussein, E., Petit, S., Churchman, J., Theng, B., Righi, D., Delvaux, B., 2005.

427   Halloysite clay minerals – a review. Clay Miner.

428   https://doi.org/10.1180/0009855054040180

429 Kim, C.H., Kim, B.-H., Yang, K.S., 2012. TiO_2 nanoparticles loaded on

430   graphene/carbon composite nanofibers by electrospinning for increased

431   photocatalysis. Carbon N. Y. 50, 2472–2481.

432   https://doi.org/10.1016/j.carbon.2012.01.069

433 Li, C., Wang, J., Feng, S., Yang, Z., Ding, S., 2013. Low-temperature synthesis of

434   heterogeneous crystalline TiO_2–halloysite nanotubes and their visible light

435   photocatalytic activity. J. Mater. Chem. A 1, 8045.

436   https://doi.org/10.1039/c3ta11176h

437 Li, C., Wang, J., Guo, H., Ding, S., 2015. Low temperature synthesis of

438   polyaniline–crystalline TiO_2–halloysite composite nanotubes with enhanced

439 visible light photocatalytic activity. J. Colloid Interface Sci. 458, 1–13.

440 https://doi.org/10.1016/j.jcis.2015.07.025

441 Mahalakshmi, M., Vishnu Priya, S., Arabindoo, B., Palanichamy, M., Murugesan, V.,

442 2009. Photocatalytic degradation of aqueous propoxur solution using TiO_2 and

443 Hβ zeolite-supported TiO_2. J. Hazard. Mater. 161, 336–343.

444 https://doi.org/10.1016/j.jhazmat.2008.03.098

445 Mamulová Kutláková, K., Tokarský, J., Kovář, P., Vojtěšková, S., Kovářová, A.,

446 Smetana, B., Kukutschová, J., Čapková, P., Matějka, V., 2011. Preparation and

447 characterization of photoactive composite kaolinite/TiO_2. J. Hazard. Mater. 188,

448 212–220. https://doi.org/10.1016/j.jhazmat.2011.01.106

449 Meng, H., Hou, W., Xu, X., Xu, J., Zhang, X., 2014. TiO_2-loaded activated carbon

450 fiber: Hydrothermal synthesis, adsorption properties and photo catalytic activity

451 under visible light irradiation. Particuology 14, 38–43.

452 https://doi.org/10.1016/j.partic.2013.04.006

453 Murgolo, S., Petronella, F., Ciannarella, R., Comparelli, R., Agostiano, A., Curri,

454 M.L., Mascolo, G., 2015. UV and solar-based photocatalytic degradation of

455 organic pollutants by nano-sized TiO_2 grown on carbon nanotubes. Catal. Today

456 240, 114–124. https://doi.org/10.1016/j.cattod.2014.04.021

457 Niu, J., Wu, A., Wang, D., Zhou, L., Zhang, S., Liu, Z., Feng, P., Ou, X., Qiang, Y.,

458 2018. Coloading of TiO_2 and C_3N_4 on kaolinite nanotubes for obviously

459 improved photocatalytic performance in degradation of methylene blue dye.

460 Mater. Lett. 230, 32–35. https://doi.org/10.1016/j.matlet.2018.07.073

461 Oliveira, H.G., Nery, D.C., Longo, C., 2010. Effect of applied potential on

462 photocatalytic phenol degradation using nanocrystalline TiO_2 electrodes. Appl.

463 Catal. B Environ. 93, 205–211. https://doi.org/10.1016/j.apcatb.2009.09.030

464 Palau, J., Colomer, M., Penya-Roja, J.M., Martínez-Soria, V., 2012. Photodegradation

465 of toluene, m -xylene, and n -butyl acetate and their mixtures over TiO_2 catalyst

466 on glass fibers. Ind. Eng. Chem. Res. 51, 5986–5994.

467 https://doi.org/10.1021/ie300357x

468 Singh, R., Dutta, S., 2018. A review on H_2 production through photocatalytic

469   reactions using TiO_2/TiO_2-assisted catalysts. Fuel 220, 607–620.

470   https://doi.org/10.1016/j.fuel.2018.02.068

471 Szczepanik, B., 2017. Photocatalytic degradation of organic contaminants over

472   clay-TiO_2 nanocomposites: A review. Appl. Clay Sci. 141, 227–239.

473   https://doi.org/10.1016/j.clay.2017.02.029

474 Wang, J.T.-W., Ball, J.M., Barea, E.M., Abate, A., Alexander-Webber, J.A., Huang,

475   J., Saliba, M., Mora-Sero, I., Bisquert, J., Snaith, H.J., Nicholas, R.J., 2014.

476   Low-temperature processed electron collection layers of graphene/TiO_2

477   nanocomposites in thin film perovskite solar cells. Nano Lett. 14, 724–730.

478   https://doi.org/10.1021/nl403997a

479 Wang, L., Zhang, C., Gao, F., Mailhot, G., Pan, G., 2017. Algae decorated TiO_2/Ag

480   hybrid nanofiber membrane with enhanced photocatalytic activity for Cr(VI)

481   removal under visible light. Chem. Eng. J. 314, 622–630.

482   https://doi.org/10.1016/j.cej.2016.12.020

483 Wang, Q., Zhang, J., Wang, A., 2013. Alkali activation of halloysite for adsorption

484   and release of ofloxacin. Appl. Surf. Sci. 287, 54–61.

485   https://doi.org/10.1016/j.apsusc.2013.09.057

486 Yuan, P., Tan, D., Annabi-Bergaya, F., Yan, W., Liu, D., Liu, Z., 2013. From platy

487   kaolinite to aluminosilicate nanoroll via one-step delamination of kaolinite:

488   Effect of the temperature of intercalation. Appl. Clay Sci.

489   https://doi.org/10.1016/j.clay.2013.08.027

490 Zhang, X., Zhou, M., Lei, L., 2005. Preparation of photocatalytic TiO_2 coatings of

491   nanosized particles on activated carbon by AP-MOCVD. Carbon N. Y. 43,

492   1700–1708. https://doi.org/10.1016/j.carbon.2005.02.013

493 Zhang, Y., Gan, H., Zhang, G., 2011a. A novel mixed-phase TiO_2/kaolinite

494   composites and their photocatalytic activity for degradation of organic

495   contaminants. Chem. Eng. J. 172, 936–943.

496   https://doi.org/10.1016/j.cej.2011.07.005

497   Zhang, Y., Guo, Y., Zhang, G., Gao, Y., 2011b. Stable TiO_2/rectorite: Preparation,

498   characterization and photocatalytic activity. Appl. Clay Sci. 51, 335–340.

499   https://doi.org/10.1016/j.clay.2010.12.023

500   Zhang, Y., Tang, Z.-R., Fu, X., Xu, Y.-J., 2010. TiO_2−graphene nanocomposites for

501   gas-phase photocatalytic degradation of volatile aromatic pollutant: is TiO_2

502   −graphene truly different from other TiO_2−carbon composite materials? ACS

503   Nano 4, 7303–7314. https://doi.org/10.1021/nn1024219

504   Zhao, D., Zhou, J., Liu, N., 2006. Characterization of the structure and catalytic

505   activity of copper modified palygorskite/TiO_2 (Cu^{2+}-PG/TiO_2) catalysts. Mater.

506   Sci. Eng. A 431, 256–262. https://doi.org/10.1016/j.msea.2006.06.001

507